Article

Reloading Mechanical Properties and Particle Flow Simulation of Pre-Peak Confining Pressure Unloading Sandstone

Bin Ma [1],*, Xinchao Ding [2] and Xingzhou Chen [3]

1   School of Civil Engineering and Architecture, Xi'an University of Technology, Xi'an 710048, China
2   Northwest Engineering Corporation Limited, Xi'an 710065, China
3   School of Architecture and Civil Engineering, Xi'an University of Science and Technology, Xi'an 710054, China
*   Correspondence: mabinyoy@163.com

Abstract: The excavation-unloading damage effects of western high-geostress slopes on rock were explored by testing the pre-peak confining pressure unloading sandstone reloading mechanical properties. The deformation and failure mechanisms were studied from a mesoscopic perspective using the particle discrete-element method. (1) Approaching the unloading failure, confining pressure increased the specimen bearing capacity attenuation. (2) The confining pressure unloading promoted microdefect propagation and development; the specimens increased rapidly to the damage stress value after reaching the initiation stress value. The penetration fracture zone was more evident and expansive in the model, and the distribution of the dense crack areas was more concentrated in the fracture zone and area. (3) The average interval of the tangential contact force was the largest in the direction of crack expansion and propagation. The strong force chains were shown to primarily bear external loads, whereas the weak force chains played a key auxiliary role in maintaining stability. (4) The number of cracks developing in the confining pressure unloading damage process indicated that the loading process did not cause damage to the specimens. The fracture zones further propagated and formed on the dominant fractures based on the damage caused by the confining pressure unloading disturbance.

Keywords: excavation unloading; damaged sandstone; confining pressure unloading; particle flow simulation; mesoscopic mechanism

1. Introduction

Many underground tunnels and slope rock masses were excavated in the processes of mineral resource exploitation, water resource construction, and hydroelectric and railway engineering. However, rock masses experience different excavation unloading damages in certain areas near the slope and tunnel excavation surfaces. During project operation and maintenance, the mechanical properties of the rock masses in the unloading zones formed by excavation and the common bearing carrier formed by the supporting structures determine the stability of the excavation project, which is a core aspect of the development and utilization of rock masses.

Generally, the rock masses in disturbed excavation unloading zones are no longer in a simple compression state, with the phenomenon of stress relief occurring along the direction of the vertical excavation surface [1], which experiences a complex stress environment. The mechanical properties of rock (masses) will be different depending on the stress environment. Scholars have conducted indoor mechanical tests on various types of rocks (masses) under complex stress environments and these can be roughly divided into loading mechanical, unloading mechanical [2], cyclic loading and unloading mechanical [3–7], and damage reloading mechanical tests [8–10]. Previous studies [11–13] conducted indoor loading tests and studied the stress–strain curves, deformation, and failure characteristics of sandstone and conglomerate specimens under various confining pressures. The unloading

mechanical tests were based primarily on conventional indoor triaxial unloading tests, considering the effects of confining pressure, unloading rate, and time on the unloading mechanical properties of rock [14–19]. Lin et al. [20] conducted triaxial loading and unloading tests on salt rock specimens and analyzed the damage characteristics and energy evolution law. Previous studies [21–23] also conducted uniaxial graded cyclic loading and unloading tests on metamorphic sandstone to examine the failure mode and the crack initiation and development process. Meng et al. [24] conducted triaxial cyclic loading and unloading tests on limestone specimens under different confining pressures and examined the strength, deformation, and expansion characteristics. Xiao [25] conducted true triaxial unloading tests on sandstone under cyclic load damage effects and examined the strength, deformation characteristics, and failure modes of sandstone under cyclic load damage effects. Meng et al. [26] prepared damaged specimens by removing the axial confining pressure and then subjected the damaged specimens to triaxial compression tests to determine the relationship between the peak stress, deformation parameters, and damage degree. Related studies [27–29] obtained damaged white sandstone and limestone specimens through triaxial loading-confining pressure unloading and then subjected them to uniaxial loading mechanical tests to examine the strength weakening mechanism and macroscopic failure characteristics. Niu et al. [30] obtained specimens with different types of initial damage by conducting loading and unloading tests on silty mudstone specimens and examined the triaxial strength characteristics of the damaged specimens under different confining pressures. In some previous studies, uniaxial compression and splitting tests were conducted on rock specimens that were first damaged before being continuously loaded and compacted [31–33].

In summary, the mechanical properties of various types of rocks under complex stress environments have been studied; however, some gaps remain in terms of understanding the excavation unloading stress environment and subsequent excavation unloading of damaged rock masses. Consequently, this study used western high-geostress rock slopes as the project background and rock (masses) in the excavation unloading disturbed zones as the research object to examine the mechanical properties of sandstone after pre-peak confining pressure unloading damage and the effect of confining pressure unloading damage on the deformation and failure characteristics of sandstone from a mesoscopic perspective using the particle discrete element method. This can provide a theoretical reference for the engineering utilization and disaster prevention of rock mass in the unloading disturbance area of rock slopes excavated with western high-geostress rock slopes.

2. Loading Test after Confining Pressure Unloading

The changes in the stress environment of rock masses in the excavation unloading disturbed zones within high-geostress rock slopes can be divided into three stages—triaxial loading, unloading, and triaxial (uniaxial) reloading. Triaxial loading corresponds to the loading state of the rock mass before excavation, unloading corresponds to the stress unloading caused by rock mass excavation, and triaxial (uniaxial) reloading corresponds to the reloading of the damaged rock mass in the unloading disturbance zone owing to the increase and transfer of peak stress in the process of graded excavation. The changing stress environment is essentially either triaxial or uniaxial loading, depending on the different confining pressures after unloading damage.

2.1. Test Scheme

The rock thermo-hydro-mechanical–chemical (THMC) multi-field coupled triaxial rheological test system was used to conduct the tests, as shown in Figure 1. We used sandstone in a west-facing high-geostress rock slope as the test material and prepared cylindrical specimens (Ø 50 × 100 mm) with the roughness values of the respective ends maintained within ±0.05 mm. We measured the densities and wave velocities of the saturated specimens, selecting specimens with relatively close values of these parameters.
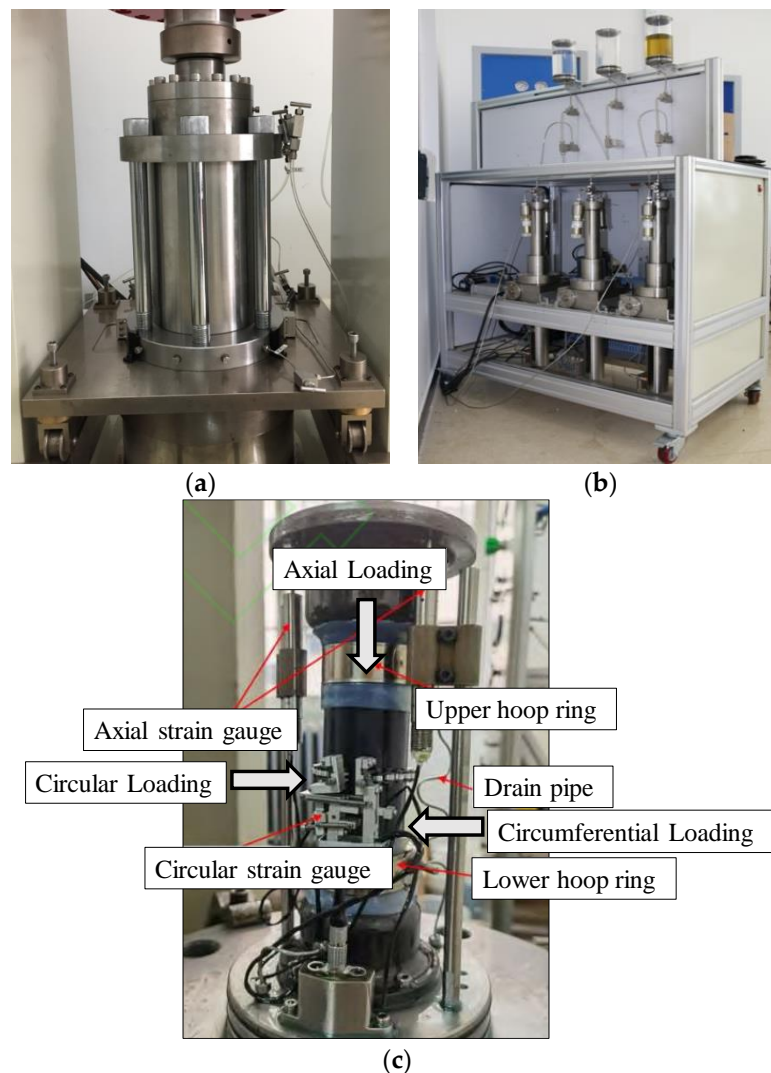
Figure 1. Thermo-hydro-mechanical–chemical multi-field coupled triaxial rheological test system:
(**a**) Confining pressure room; (**b**) Axial pressure and confining pressure servo device; (**c**) Loading
cylinder diagram.

2.1.1. Conventional Uniaxial and Triaxial Loading (Unloading) Tests

1. Triaxial loading test: The stress control mode was adopted, setting the target value
of the confining pressure to 25 MPa. The following specific process was applied.
(a) In the hydrostatic pressure stage, the loading rate of the confining pressure
and axial pressure was maintained at 1.5 MPa/min until the confining pressure
reached the target value. (b) The confining pressure was maintained at a constant
value, and the axial pressure was loaded at 3 MPa/min until the specimen was de-
formed and failed to obtain the triaxial compressive strength under the corresponding
confining pressure.

2. Triaxial unloading test: The stress control mode was adopted, setting the target value
of the axial pressure to 55% of the corresponding triaxial compressive strength. The
following specific process was used. (a) The hydrostatic pressure stage used in the tri-
axial loading test was applied. (b) The confining pressure was maintained at a constant
value of 25 MPa; then, the axial pressure was loaded to 55% of the triaxial compressive
strength at 3 MPa/min. (c) The axial pressure was maintained at a constant value,
and the confining pressure was loaded at 1.5 MPa/min until the specimen deformed
and failed.

2.1.2. Preparation and Loading Tests of Pre-Peak Confining Pressure Unloaded Specimens

A control group was set up to unload the sample without pre-peak confining pressure.

The following process was used to prepare the pre-peak confining pressure unloading specimens: (a) Under the same loading process as the triaxial loading test, the axial pressure was maintained at a constant value after the target value was reached; then, the confining pressure was reduced to 20 MPa at 1.5 MPa/min. (b) The axial pressure was then unloaded at 1.5 MPa/min to the same value as the confining pressure (20 MPa). (c) The axial and confining pressures were unloaded simultaneously at 1.5 MPa/min to complete the preparation of the 5 MPa confining pressure unloading specimens. Specimens with confining pressures reduced to 15 MPa and 10 MPa could also be obtained in this manner. Uniaxial and triaxial reloading tests were conducted with 15 MPa confining pressure.

2.2. Results Analysis

The specimens were subjected to uniaxial compression at σ_0 = 86.5 MPa, 25 MPa confining pressure triaxial compression at σ_{25} = 167.8 MPa. All failed when the confining pressure was unloaded to approximately 6.3 MPa and 5 MPa confining pressure triaxial compression at σ_{15} = 142.3 MPa.

Evidently, from Figure 2, the loading triaxial stress–strain curves of the specimens under different confining pressure unloading are similar and can be roughly divided into four stages: fracture compaction, elastic deformation, plastic deformation (deformation and failure development), and post-peak. (a) In the fracture compaction stage, the primary cracks and pores in the specimens were compressed and closed by the deviatoric stress. (b) In the elastic deformation stage, the stress–strain curve is linear and the properties are stable. (c) In the plastic deformation (deformation and failure development) stage, the specimen entered the plastic stage and the stress–strain curve began to deviate from a straight line, with the slope decreasing gradually as microcracks in the specimen continued to develop until the peak stress state was reached. (d) In the post-peak stage, the internal cracks propagated after the specimen reached its peak stress and converged rapidly to form macroscopic fractures, leading to failure of the specimen.
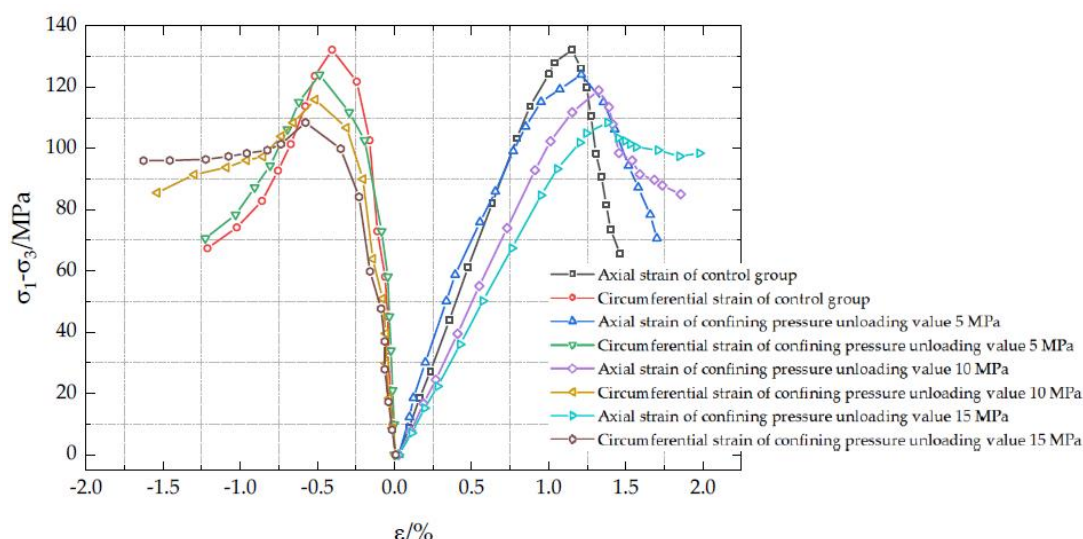
Figure 2. Triaxial reloading stress–strain relationship curves of confining pressure unloading specimens.

Figure 3 shows the peak strain–confining stress curve. Evidently, the peak strain increased with the confining pressure unloading, with the axial peak strain increasing by 5.2, 15.0, and 20.0% and the circumferential peak strain increasing by 20.0, 29.6, and 42.5%, respectively, compared with the case in which the confining pressure unloading was zero. The circumferential peak strain was more sensitive to the response of confining pressure unloading damage effects.
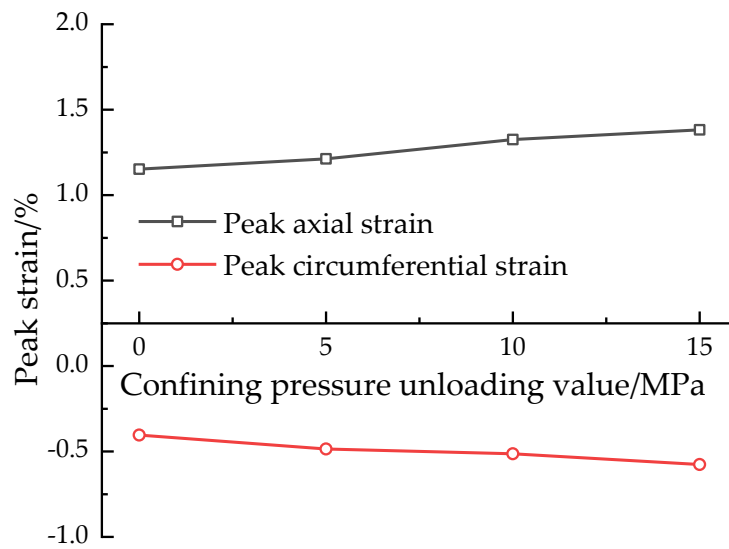
Figure 3. Peak strain–confining pressure unloading curve.

The crack volume strain model proposed by Martin [34] can be used to analyze the crack initiation stress (σ_{ci}) and damage stress (σ_{cd}), with the axial stress corresponding to the starting point of the stable crack propagation stage assumed to be equivalent to the initiation stress (σ_{ci}) and the axial stress corresponding to the starting point of the accelerated crack propagation stage assumed to be equivalent to the damage stress (σ_{cd}).

As shown in Figure 4 and Table 1, the initiation stress (σ_{ci}) decreased by 8.8, 20.6, and 41.1%, whereas the damage stress (σ_{cd}) decreased by 9.6, 19.9, and 37.8%, respectively compared with the case in which the confining pressure unloading was zero. In contrast, the initiation stress (σ_{ci}) decreased more when the confining pressure unloading was larger; it was more sensitive to confining pressure unloading. The differentials between the initiation stress (σ_{ci}) and damage stress (σ_{cd}) also decreased. This indicates that microdefects such as microcracks, grain boundaries, and lattice defects in the rock specimens will propagate and develop when the stress environment changes. Consequently, the stress of the specimens increased rapidly to the damage stress value after reaching the initiation stress value; the stable crack propagation stage was shortened and the bearing capacity was reduced.
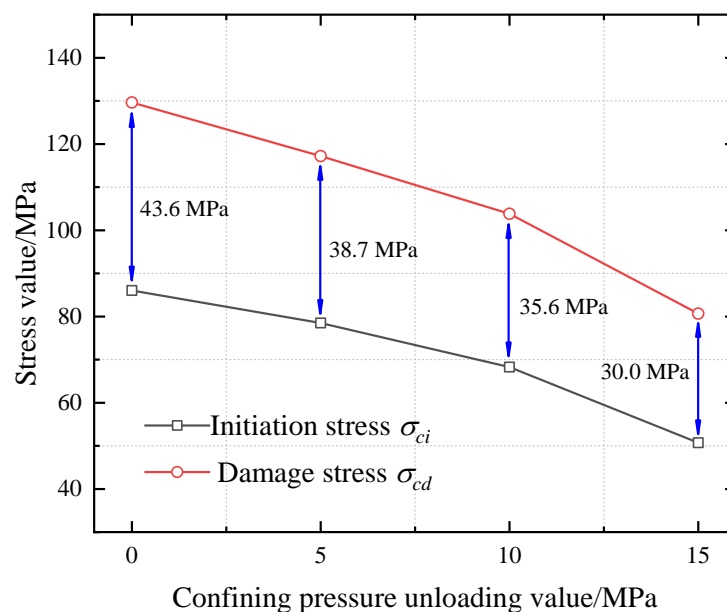

Figure 4. Initiation/damage stress–confining pressure unloading curve.

Table 1. Differentials between the initiation stress (σ_{ci}) and damage stress (σ_{cd}).

Differentials	Confining Pressure Unloading 0 MPa	Confining Pressure Unloading 5 MPa	Confining Pressure Unloading 10 MPa	Confining Pressure Unloading 15 MPa
σ_{cd}-σ_{ci}	43.6	38.7	35.6	30.0

Figure 5 reveals that confining pressure unloading affects the strength, which decreases as the confining pressure unloading increases. When the confining pressure unloading was 15 MPa, the decrease was more evident, with the uniaxial and triaxial compressive strengths decreasing by 18.6% and 13.4%, respectively, compared with the case in which the confining pressure unloading was zero. This is because the specimens all failed by the point where the confining pressure was unloaded to 6.3 MPa; when the confining pressure was unloaded to 10 MPa (with an unloading of 15 MPa), it is close to the failure value of the confining pressure unloading, and the internal structures of the specimens were persistently damaged. These damages accumulated, resulting in crack propagation and development, and leading to a considerable decrease in strength. Additionally, the confining pressure had an inhibitory effect on the decrease in the strength of the specimen.
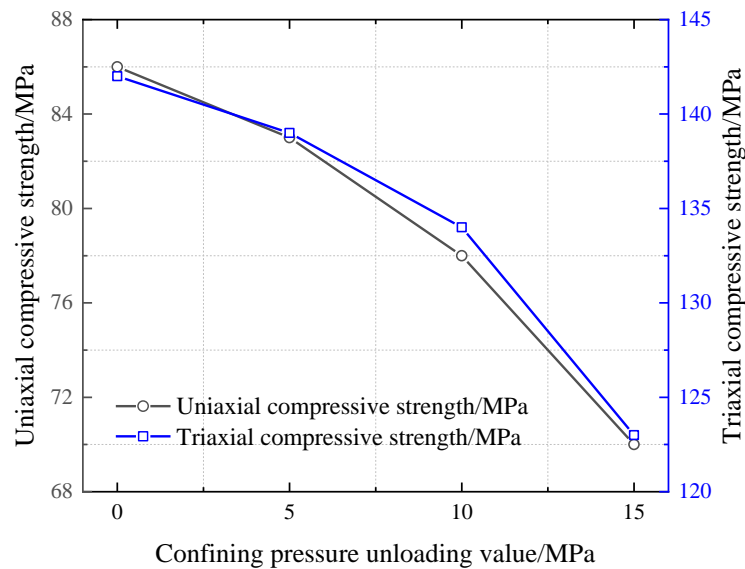
Figure 5. Reloading uniaxial/triaxial compressive strength–confining pressure unloading curve.

Wang et al. [35] defined the triaxial compressive initiation stress level (*K*) of rock, which reflects the discrete characteristics and structural differences. When *K* decreases, the heterogeneity of the rock increases, which can be expressed as follows:

$$K = \frac{\sigma_{ci}}{\sigma_s} \tag{1}$$

where *K* denotes the triaxial compressive initiation stress level and (σ_s) denotes the triaxial compressive strength under the corresponding confining pressure.

An analysis of Table 2 shows that increasing the unloading induces the internal particles of the specimens to move and collide as a result of confining pressure unloading damage. This causes a gradual structural transition to coarse, large particles, which in turn causes *K* to decrease. From a macro perspective, excavation unloading is the main factor for inducing the changing mechanical properties of slope rock masses, aggravating the propagation and development rate of internal cracks, and weakening their mechanical properties in the excavation unloading disturbed zones.

Table 2. *K* values corresponding to different levels of confining pressure unloading.

Initiation Stress Level	Confining Pressure Unloading 0 MPa	Confining Pressure Unloading 5 MPa	Confining Pressure Unloading 10 MPa	Confining Pressure Unloading 15 MPa
K	0.61	0.56	0.51	0.41

3. Particle Flow Simulation

3.1. Simulation Scheme

PFC^{2D} particle flow software was used for the simulation via a particle contact model based on the commonly used linearpbond model, which effectively reflects the failure characteristics of rock materials. The 100×50 mm numerical model is shown in Figure 6. The stress path set in the simulation was the same as that used in the laboratory test. The confining pressure loading of 15 MPa was applied to the control group, and triaxial loading (confining pressure 25 MPa) $\rightarrow$ confining pressure unloading (unloading 5, 10, and 15 MPa) and triaxial reloading (confining pressure 15 MPa) were applied to the test group. The loading rate in the PFC^{2D} software was not the same as that applied in the laboratory test because of its high default damping coefficient. A typical quasi-static simulation can be conducted at high speeds with a loading rate of 0.15 m/s. The stop condition of the simulation calculation was triggered when the post-peak axial stress was approximately 40% of the triaxial compressive strength.
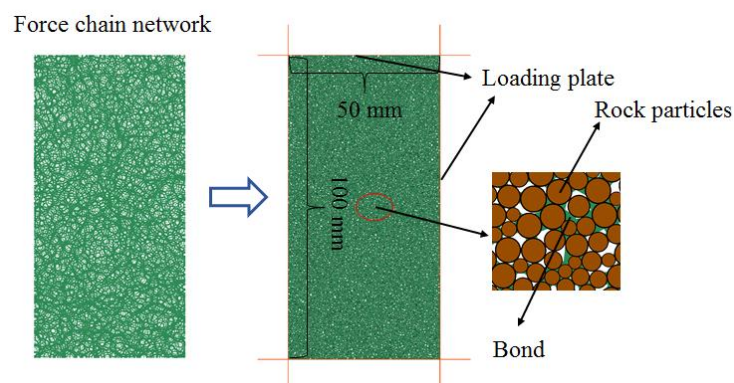

Figure 6. Numerical simulation model.

3.2. Parameter Calibration

The linearpbond contact model was used to simulate the properties of sandstone matrix materials. The model is mainly used to simulate the mechanical behavior of particle cementing materials and has good adaptability to simulate rock. The linearpbond model contains two contact interfaces. The first is an infinitely small elastic interface, which does not bear tension and only transmits force. The second is a linear elastic bonding interface, which can resist torque. When the force of the linear elastic bonding interface exceeds the strength limit, the bonding interface is destroyed and only the elastic interface remains. At this time, the model is equivalent to the linear model, as shown in Figure 7.

The contact bonding state of particles in the PFC^{2D} model determines the macroscopic mechanical response of the material, whereas the contact bonding state is determined by mesomechanical parameters such as the bonding modulus and strength.

Consequently, the ideal macroscopic deformation and failure in the simulation were determined through trial and error accompanied by calibration of the mesoparameter set. The stress–strain relationship curve shown in Figure 3 was used as the basis for the calibration. The mesomechanical parameters obtained from the final calibration are listed in Table 3. The stress–strain relationship curves, hotspot and distribution diagram of cracks, the average contact force and normal statistics, force chain structure diagram, moment magnitude distribution, and statistics diagram were obtained using FISH programming.

(a)

(b)
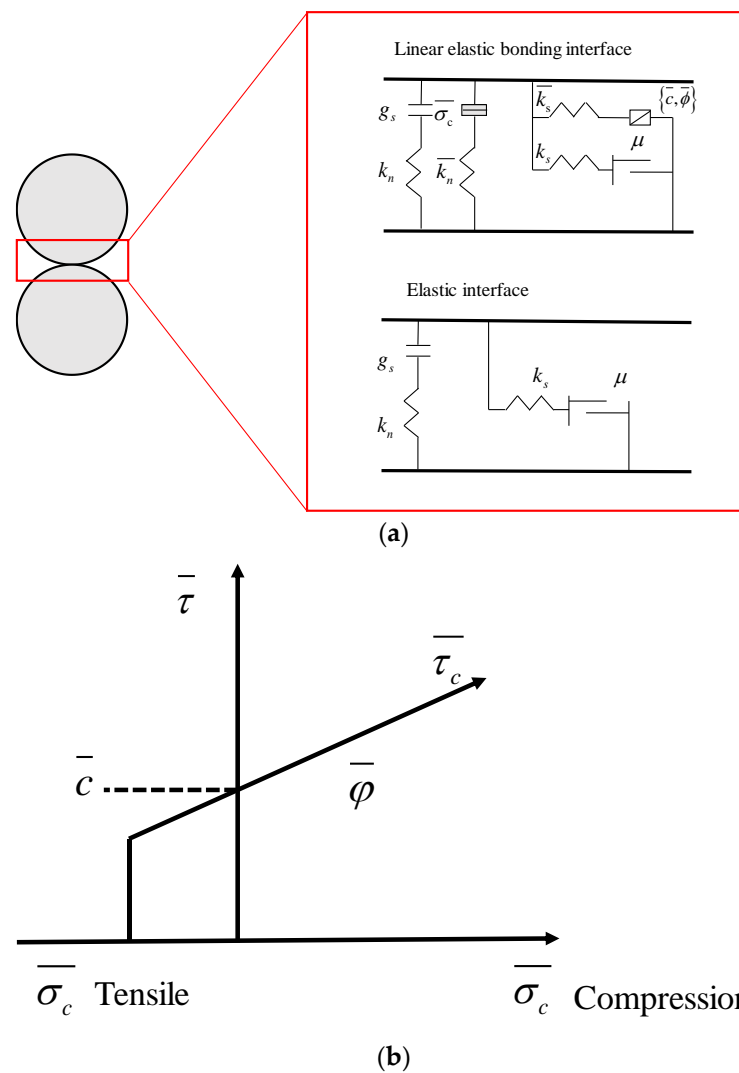
Figure 7. Linearpbond model diagram and failure envelope line: (**a**) Linearpbond model schematic diagram; (**b**) Linearpbond model failure envelope. $\overline{k_s}$—Bond tangential stiffness; $\overline{k_n}$—Bonding normal stiffness; $\overline{\sigma_c}$—Tensile strength; $\overline{\tau}/\overline{\tau_c}$—Shearing strength; $\overline{c}/\overline{\varphi}$—Cohesion and friction angle; μ—coefficient of friction; g_s—Bond activation gap; k_n—Normal stiffness; k_s—Tangential stiffness.

Table 3. Main mesomechanical parameters.

Simulation Scheme	Contact Modulus/GPa	Contact Tensile Strength/MPa	Contact Cohesion/MPa	Other Parameters
Control group	2.30	42.75	42.75	Particle modulus 23/GPa
Confining pressure unloading 5 MPa	1.84	40.5	39.9	Density 2500 kg/m^3 Minimum particle size 0.25/mm
Confining pressure unloading 10 MPa	1.29	35.7	37.8	Maximum particle size 0.5/mm Particle stiffness ratio 3
Confining pressure unloading 15 MPa	0.97	31.92	33.18	Contact stiffness ratio 3 Particle friction coefficient 0.6

The simulated stress–axial strain and error rate curves are shown in Figure 8. The peak stress error interval is −1.85% to 2.42% and the peak strain error interval is −1.72% to 2.27%, both of which are maintained within 3%. The simulated results are consistent with the actual results, indicating that the setting of the mesomechanical parameters was reasonable.

PFC^{2D} can be used to study the effect of confining pressure and unloading damage on the deformation and failure characteristics of sandstone from a mesolevel perspective.
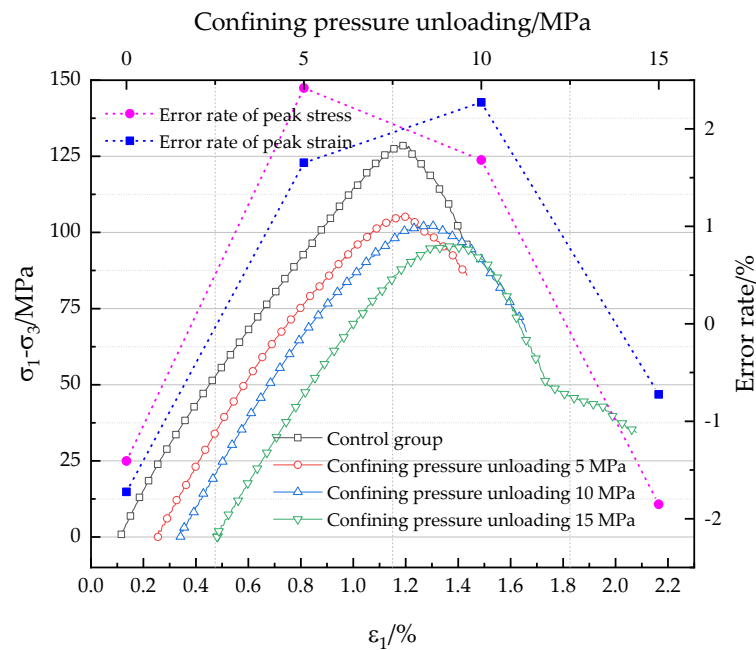
Figure 8. Loading axial stress—axial strain and error rate curves. Error rate = (measured value − simulated value)/measured value × 100%.

3.3. Result Analysis

The contact between particles will be destroyed as a result of the bond-breaking failure induced by external loads. By monitoring and analyzing the cracks generated in the simulation process, the internal fracture gestation, development, and evolution process of the model can be determined. Figure 9 shows a hot spot map of the cracks occurring in the case of model failure.
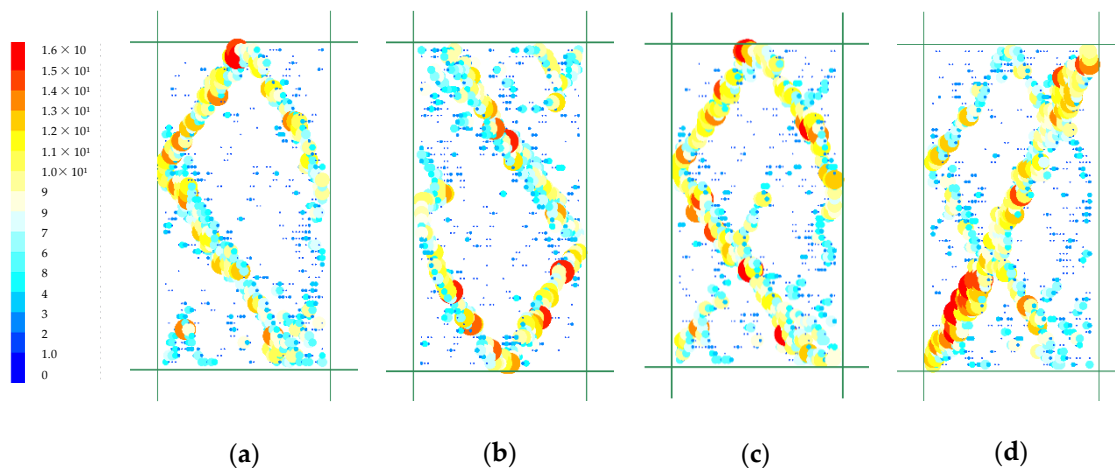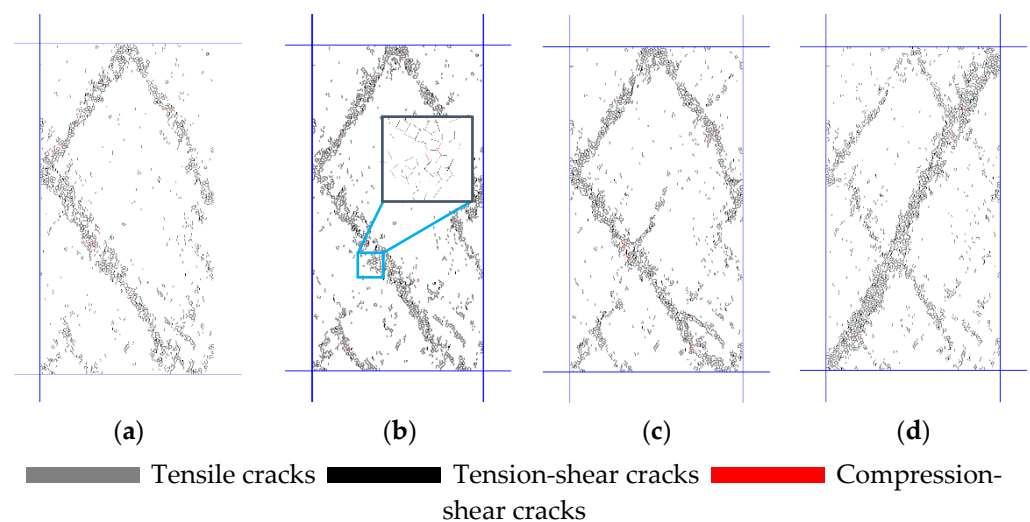

Figure 9. Hot spot map of cracks in the case of model failure: (**a**) Control group; (**b**) Confining pressure unloading of 5 MPa; (**c**) Confining pressure unloading of 10 MPa; (**d**) Confining pressure unloading of 15 MPa.

Figure 9 reveals that the areas with dense cracks changed with increasing confining pressure unloading. In the control group model, three fissure zones exhibited penetration trends. When the confining pressure unloading was 5 MPa, the cracks were concentrated in the lower right part of the map, a slight fracture zone was sandwiched in the upper

shoulder right part, and the penetration fissure zone became increasingly apparent as the dense crack area began to propagate into the model. When the confining pressure unloading was 10 MPa, the cracks developed inward continuously, with the cracks in the corner and bottom continuing to densify; the cracks in the upper right corner and lower left bottom began to interpenetrate the internal cracks, and the main fracture zone exhibited a diagonal penetration trend. When the confining pressure unloading was 15 MPa, the cracks gradually propagated from the middle to both sides, with the cracks in the middle, both sides, and ends being more concentrated and a more apparent fracture zone formed along the diagonal. Overall, increasing the confining pressure unloading caused dense crack areas to become more concentrated in the fracture zone and fracture area.

Figure 10 shows the distribution of different types of cracks when the model has failed, and Figure 11 shows the corresponding statistical curves. It is evident from the figures that the distribution of cracks is consistent with the hot-spot distribution of cracks, with a large number of cracks concentrated in certain areas or distribution zones, which can be macroscopically shown as shear or tensile crack zones. The ratio of shear to tensile cracks was approximately 1:15–1:10 and the tensile cracks were dominant, with only a few shear cracks. The number of compression-shear cracks was relatively small (between 20 and 30). Tension-shear and shear cracking first decreased before increasing, presumably because the confining pressure unloading value of 5 MPa was small; the unloading confining pressure ratio was only 26.8%. The model was compacted, resulting in a decrease in tension-shear cracking. Increasing the confining pressure unloading caused the total number of cracks to gradually increase, with test-group crack growths of 8.6%, 16.1%, and 30.0% relative to the control group, indicating that confining pressure unloading promotes fracture deformation in the specimens. Moreover, there are tension-shear and compression-shear cracks around the tensile cracks, as the tensile cracking in the early stages of the model is usually followed by cracking along the shear plane. It can be surmised that the deformation and failure were caused primarily by pressure-induced tensile fracturing and hence, can be considered to be brittle shear failure. Overall, the number of compression-shear cracks was small, indicating that increasing the unloading causes the mode of model failure to gradually transition to tension-shear and tensile failure.

(**a**) (**b**) (**c**) (**d**)

▬ Tensile cracks ▬ Tension-shear cracks ▬ Compression-shear cracks

Figure 10. Distributions of different types of cracks. (**a**) Control group (**b**) Confining pressure unloading value 5 MPa (**c**) Confining pressure unloading value 10 MPa (**d**) Confining pressure unloading value 15 MPa.
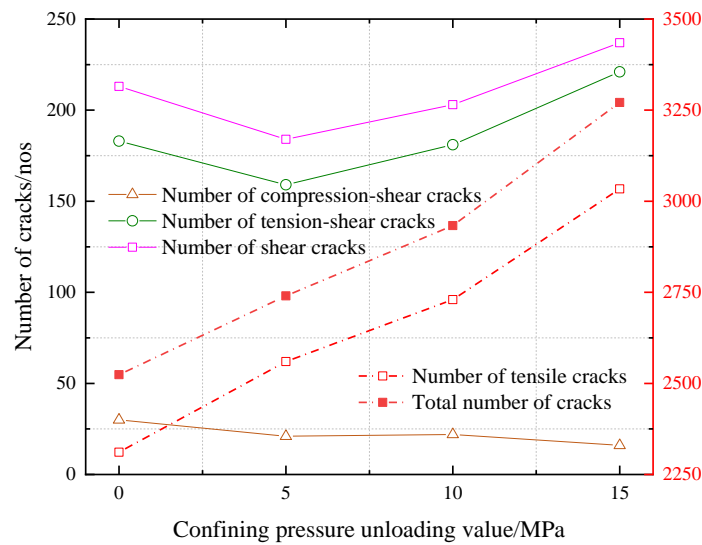
Figure 11. Statistical curves of different types of cracks.

The changes in the geometric (contact force network shape) and mechanical structures (force chain structure shape) of the particles in mesostructures are closely related to the macroscopic mechanical properties of the model. To reflect this, the distributions of the normal, average normal, and average tangential contact forces between the model particles are plotted in Figures 12 and 13.
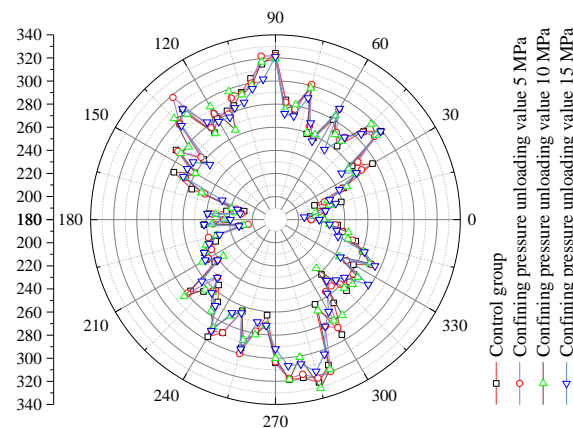

Figure 12. Normal statistical curve of contact force.

Evidently, the normal statistical curve of the contact force is approximately "spindle-shaped", and the anisotropic mechanical behavior is apparent, with a rigid rotation between particles that was relatively strong under loading. The fluctuation was relatively strong in the 150–210° range and more pronounced in the vertical axial direction (near 90° and 270°) than in the horizontal direction (near 0° and 180°), indicating that the model primarily bears vertical loading, which is consistent with the actual test results.

The total number of normal contact forces decreased gradually from 19,451→19,438 →19,397→19,165 as the contact fracturing of particles increased and the damage degree intensified. The average tangential contact forces in the 45–75°, 105–135°, 225–250°, and 270–300° intervals increased but diminished in the horizontal direction to within 10 N. There is a correlation between the average tangential contact force and the crack distribution, particularly in the 15 MPa confining pressure unloading case where the average tangential contact force was larger in the 45–60°, 225–240°, and 285–300° intervals corresponding to the directions of concentrated crack propagation. The average normal contact force was larger in the 105–120° and 270–285° intervals, which is consistent with the loading direction of the model.
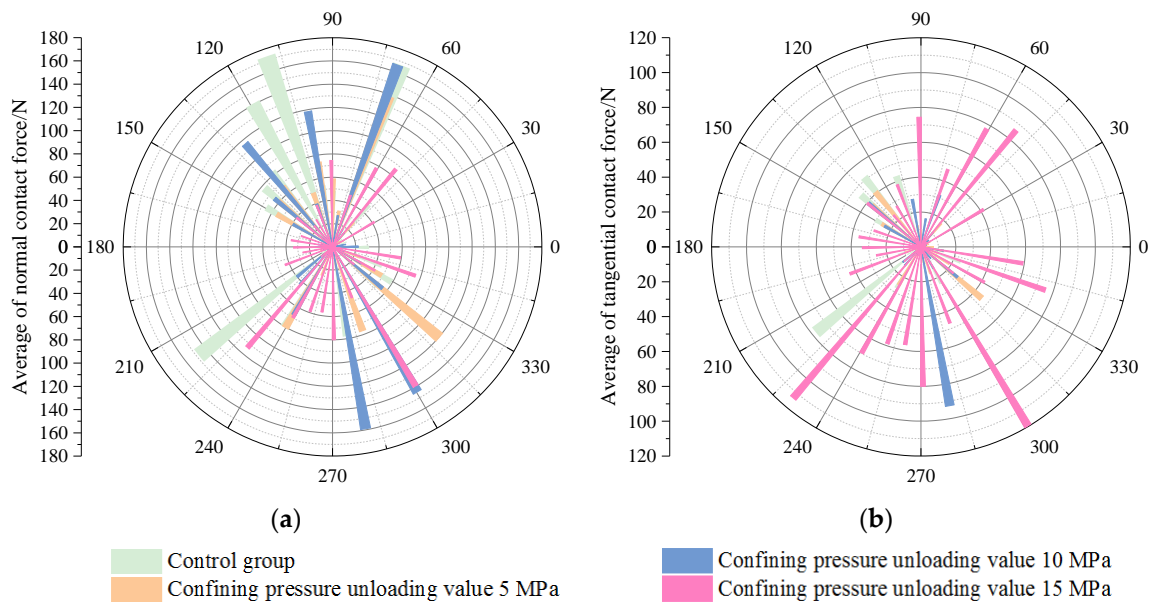
Figure 13. Statistical diagram of the average contact force: (**a**) Average of normal contact force; (**b**) Average of tangential contact force.

Overall, the normal contact force was greater than the average tangential contact force; however, with increasing confining pressure unloading, the average normal contact force decreased, indicating that the normal contacts between particles weakened and the particles were gradually stretched. Meanwhile, the mean tangential contact force increased and began to exhibit shear dislocation deformation primarily in the 30–60°, 210–240°, and 270–300° intervals, with the average value increasing to 100–120 N, which is consistent with the distribution of the fracture zone. This is possibly related to the decrease in the unloading path of σ_3 in the process of confining the pressure unloading damage.

The standardized normal contact force can be used to analyze the relationship between the force chain network shape and the deformation and failure of a model. When the standardized normal contact force of a contact is greater than the average normal contact force in the region, it can be considered a strong force chain; otherwise, it can be considered a weak force chain. The standardized normal contact force can be defined as

$$f = \frac{f_n}{\overline{f_n}} \tag{2}$$

where f denotes the standardized normal contact force, f_n denotes a single normal contact force, and $\overline{f_n}$ denotes the average normal contact force of the model.

Figure 14 shows the standardized force chain shape diagram of the model. Evidently, the distributional shape of the force chains in a specimen characterizes the conduction process of the force, with the shapes of the force chains under different scheme failures being clearly different. Increasing the unloading caused strong force chains (thicker lines) to run through the model and the bearing capacity of the specimen to weaken gradually. Although the pressure and tension chains were distributed throughout the overall particle system, the performance of the pressure chains is more apparent, indicating that the state of the pressure-induced tensile fracturing constitutes the basic form of deformation and failure. However, the strong force chains, which primarily bear external loads, accounted for approximately 40% of the total number of force chains. The weaker force chains are distributed around and connect with the strong force chains, which can bear less tangential force and only part of the load but play a key auxiliary role in the stability of the strong force chains.
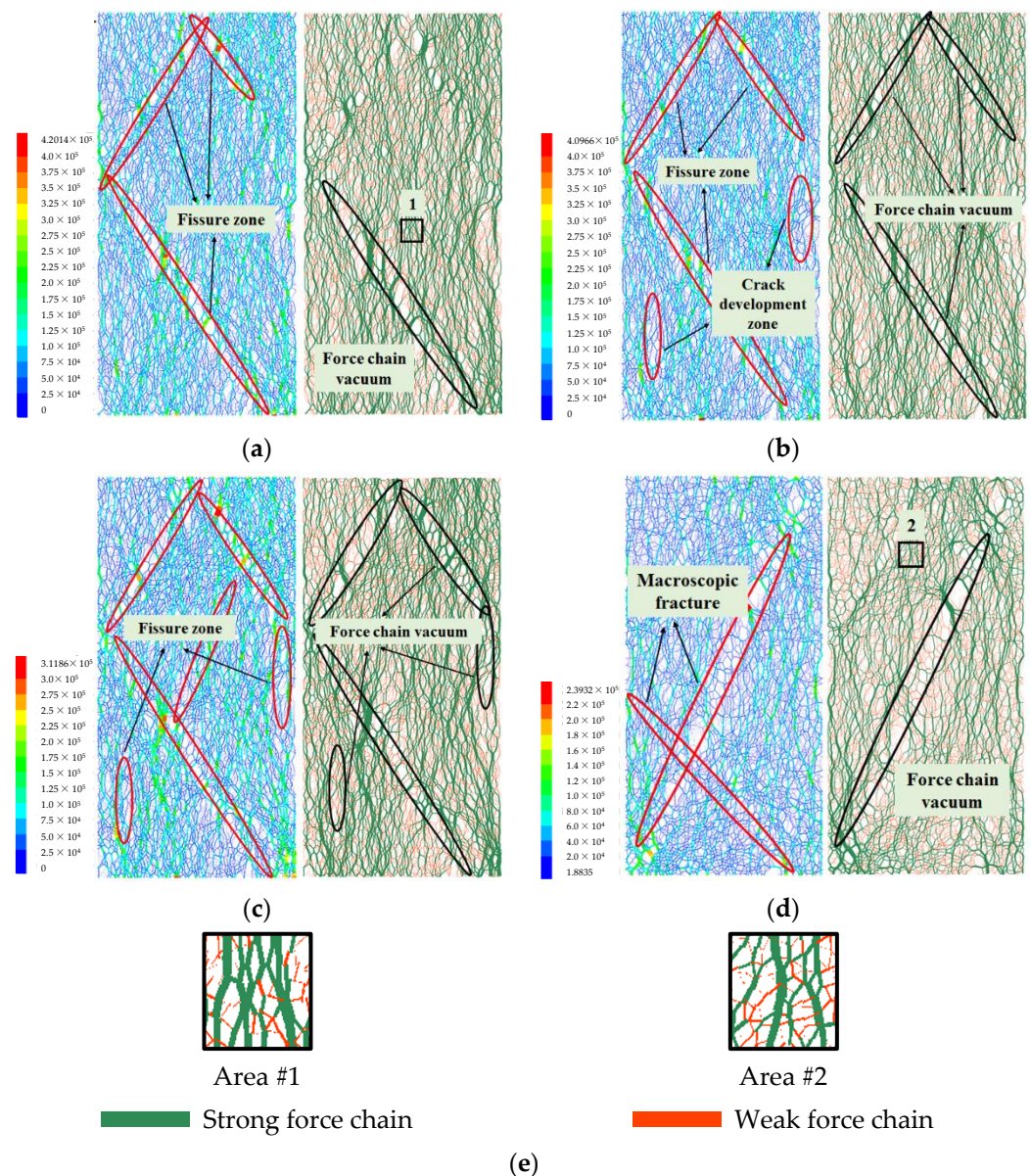
Figure 14. Standardized force chain shape diagram: (**a**) Control group; (**b**) Confining pressure unloading of 5 MPa; (**c**) Confining pressure unloading of 10 MPa; (**d**) Confining pressure unloading of 15 MPa; (**e**) Enlarged diagram of the force chain structure.

In the fissure or macroscopic fracture zone, the strong force chains were more concentrated, and the contact force chains were more densely distributed, exhibiting a circular and crisscross network distribution and forming a dense network force chain structure. The number of strong force chains changed from 7787→7825→7807→7272; that is, they first increased and then decreased, which is consistent with changes in the number of shear cracks, a decrease in the maximum pressure of particle contact, a gradual increase in the number of buckling of force chains, and the tendency of the strong force chains to shift toward the direction of confining pressure. This pattern, combined with the information in the crack distribution and test failure images, indicated that macroscopic fractures occur in the vacuum areas of the force chains where the deformation differences are large.

4. Discussion

When preparing pre-peak confining pressure unloading specimens, triaxial loading of the specified confining pressure and axial pressure should be performed first. If the set axial pressure is significantly high, it will cause loading damage to the specimen, interfering with the subsequent confining pressure unloading damage process. Therefore, appropriate selection of the specified axial pressure value is particularly important to ensure that the damage to the specimen is solely caused by confining pressure unloading.

Table 4 presents a comparison of the number of cracks that occurred in the specimens under different unloading pressure conditions. No cracks were observed on loading to 55% of the triaxial compressive strength. When the confining pressure unloading was 15 MPa, the number of cracks was 381, indicating an apparent increase of 34.6 and 6.7 times occurring under confining pressure unloadings of 5 MPa (11) and 10 MPa (57), respectively. These results indicate that under a triaxial loading process with a set confining pressure and axial compression, the loading did not cause damage; instead, the damage was induced by the confining pressure loading.

Table 4. Number of confining pressure unloading cracks under different confining pressure unloading conditions.

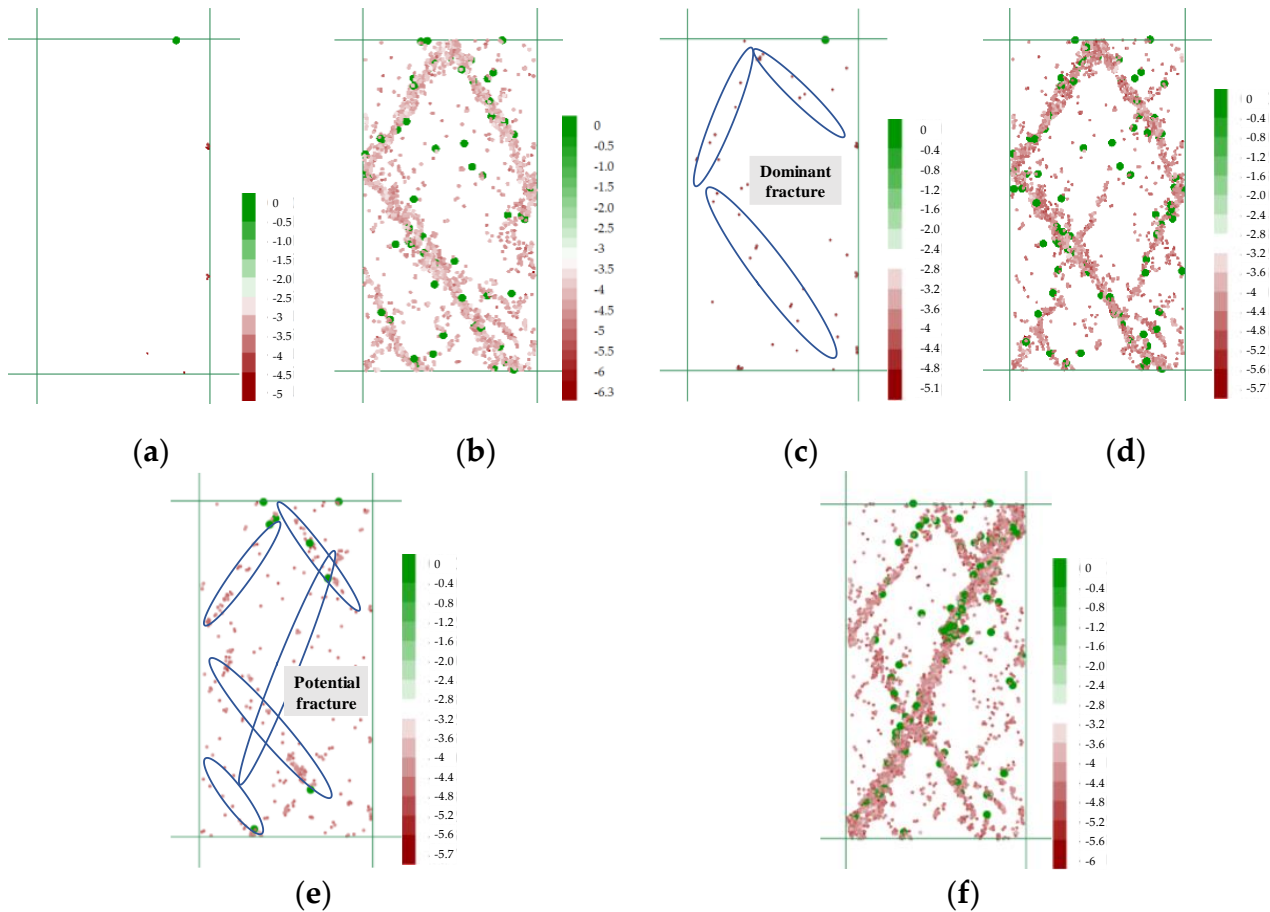| Confining Pressure Unloading Conditions	Loaded to 55% of Triaxial Compressive Strength	Confining Pressure Unloading 5 MPa	Confining Pressure Unloading 10 MPa	Confining Pressure Unloading 15 MPa
Number of cracks/nos	0	11	57	381

The confining pressure unloading is closely related to the final deformation and failure of the model. To describe and analyze the relationship between them as quantitatively as possible, we used simulated acoustic emission for the analysis. The moment magnitude of the acoustic emission event caused by the breaking of a bond can be calculated by monitoring the changes in the contact force around the fault source particles. The moment magnitude reflects the failure intensity of the fracture event, characterizing the dislocation of the fault surface caused by each event and the energy released as a result. The moment magnitude calculation formula is expressed as follows [36]:

$$M = \frac{2}{3}\lg M_0 - 6 \tag{3}$$

where M_0 denotes the scalar moment, $M_0 = \left(\frac{1}{2}\sum_{j=1}^{3} m_j^2\right)^{1/2}$, and m_j denotes the characteristic value of the moment tensor matrix.

It is evident from the distribution of moment magnitudes in Figure 15 that increasing the confining pressure unloading causes the moment magnitude distribution to change from a random scattered distribution to a regular accumulation. In this process, the degree of damage is continuously strengthened in a manner closely related to the final fracture shape. In the case of bond fracture failure, the particles on both sides of the fracture produce a larger energy release—the damage is intensified as the moment magnitude decreases—which leads to surrounding dislocation deformation and causes the adjacent bonds to break, resulting in the initiation of microcracks, with a number of similar microcracks accelerating and converging to form crack clusters. When the number of microcracks increased to a certain level, the adjacent microcrack clusters propagated and connected to form dominant fractures, and the moment magnitude decreased gradually. For instance, the dominant fracture moment magnitude shown in Figure 15c is approximately -3.8, whereas the potential fracture moment magnitude shown in Figure 15e is approximately -4.2, with the moment magnitude concentration in the potential fracture area being more evident and the total microcrack initiation increasing rapidly. In the subsequent triaxial

loading process, the dominant fractures evolved into a relatively well-defined macroscopic fracture zone. Finally, the fracture zone was further propagated, forming the basis for the damage caused by confining pressure unloading disturbance.

Figure 15. Moment magnitude distribution diagram of the model: (**a**) Confining pressure unloading of 5 MPa; (**b**) Confining pressure unloading of 5 MPa causing loading damage; (**c**) Confining pressure unloading of 10 MPa; (**d**) Confining pressure unloading of 10 MPa causing loading damage; (**e**) Confining pressure unloading of 15 MPa; (**f**) Confining pressure unloading of 15 MPa causing loading damage.

Figure 16 shows the statistical frequencies and proportional distributions of the moment magnitude values. It can be observed that the moment magnitude of confining pressure unloading damage is concentrated primarily in the -5.0 to -4.0 range, corresponding to a change in the number of acoustic emissions from $8 \rightarrow 51 \rightarrow 322$, which accounts for approximately 90–95% of the total number of acoustic emissions and a change in the average moment magnitude from $-4.42 \rightarrow -4.49 \rightarrow -4.53$. In the final deformation and fracture process, the moment magnitude is concentrated primarily in the -5.5 to -3.5 range, corresponding to a change in the number of acoustic emissions from $2158 \rightarrow 2377 \rightarrow 2690$, accounting for approximately 95% of the total number of acoustic emissions and a change in the average moment magnitude from $-4.28 \rightarrow -4.31 \rightarrow -4.35$. It is evident that the number of acoustic emissions increases with the magnitude of confining pressure unloading as well as an expansion of the distribution range of the moment magnitude and a decrease in the average moment magnitude, indicating that the overall damage degree of bonding fracturing in the model gradually intensifies.
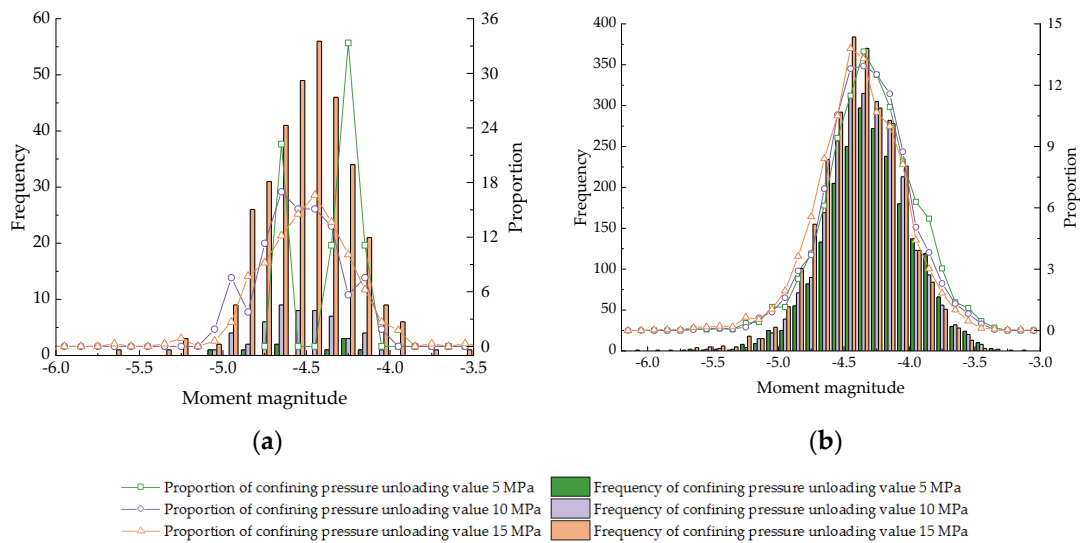
Figure 16. Statistical frequency and proportional distribution of moment magnitude values. (**a**) Confining pressure unloading damage, (**b**) Loading after confining pressure unloading damage.

5. Conclusions

The deformation and failure law of sandstone after confining pressure unloading damage was studied using laboratory tests and numerical simulation. This can be used to effectively analyze the structural damage changes of sandstone in the process of reloading after confining pressure unloading from a microscopic perspective such as the crack hot spot, force chain structure, and moment magnitude. The main conclusions drawn based on the findings of the study are summarized below.

1. There was a positive correlation between the confining pressure unloading and the peak strain, with the circumferential peak strain proving to be more sensitive to confining pressure unloading damage effects. A negative correlation was observed between the strength of a specimen and its confining pressure unloading. The decrease in strength was more apparent as the unloading failure confining pressure approached. Confining pressure had a certain inhibitory effect on the attenuation of the bearing capacity of the specimens.

2. The initiation stress (σ_{ci}) decreased more than the damage stress (σ_{cd}) with increasing confining pressure unloading. The microdefects in the specimens further propagated and developed under confining pressure unloading conditions, shortening the stable crack propagation stage; the differences between the initiation stress (σ_{ci}), damage stress (σ_{cd}), and triaxial compressive initiation stress level (*K*) also decreased.

3. With a gradual increase in the confining pressure unloading, the penetration fracture zone was more evident and expansive in the model, and the distribution of dense crack areas was more concentrated in the fracture zone and fracture area. The total number of cracks increased, with tensile cracks being dominant and accompanied by tension-shear and compression-shear cracks as a result of deformation and failure caused by pressure-induced tensile fractures.

4. The anisotropic mechanical behavior of the model was evident under deformation and failure, with increases in bond breaking, weakening of the normal contact force, and enhancement of the tangential contact force, all of which led to serious damage. The average interval of the tangential contact force was the largest in the direction of crack expansion and propagation. The strong force chains were shown to primarily bear external loads, whereas the weak force chains played a key auxiliary role in maintaining stability. Macroscopic fractures occurred easily in the vacuum areas of the force chains.

5. The number of cracks developing in the confining pressure unloading damage process indicated that the loading process did not cause damage to the specimens. The

moment magnitude distributions changed from randomly scattered distributions to regular accumulations, with dominant fractures accumulating to form potential fractures. Finally, fracture zones further propagated and formed on the dominant fractures based on the damage caused by confining pressure unloading disturbance. Increasing levels of acoustic emissions caused the distributional range of the moment magnitude to expand and the average moment magnitude to decrease, indicating that the overall degree of damage caused by bonding fractures in the model gradually intensified.

References

1. Huang, D.; Huang, R.Q. Physical model test on deformation failure and crack propagation evolvement of fissured rocks under unloading. *Chin. J. Rock Mech. Eng.* **2010**, *29*, 502–512.
2. Duan, Y.; Zhang, G.; Qin, T. Analysis of crack-characteristic stress and energy characteristics of sandstone under triaxial unloading confining pressure. *Appl. Sci.* **2023**, *13*, 2671. [CrossRef]
3. Wang, C.; Zhao, Z.; Zuo, C. Energy behaviour of coal failure under uniaxial cyclic loading/unloading. *Appl. Sci.* **2023**, *13*, 4324. [CrossRef]
4. Luo, J.A.; Wang, L. Study on energy evolution and damage constitutive model of sandstone under cyclic loading and unloading. *Appl. Sci.* **2023**, *13*, 1690. [CrossRef]
5. Gao, S.; Meng, H.; Wu, Y.; Wang, X.; Wang, Y.; Wu, J.; Wang, P. Examination of the effects of different frequencies on rock fracturing via laboratory-scale variable amplitude fatigue loading experiments. *Appl. Sci.* **2023**, *13*, 4908. [CrossRef]
6. Gao, M.; Yan, H.; Duan, H.; Xiong, S. Experimental study on coal specimens subjected to uniaxial cyclic loading and unloading. *Appl. Sci.* **2022**, *12*, 11810. [CrossRef]
7. Zhong, P.; Li, J.; Zhou, X.; Xiao, H.; Yue, S.; Zhang, P.; Wang, Y. Study of energy evolution law and damage characteristics during uniaxial cyclic loading and unloading of sandstone. *Appl. Sci.* **2022**, *12*, 9985. [CrossRef]
8. Chen, X.; Du, W.; Chen, L.; Ma, B.; Gong, S.; Jiang, H.; Wang, W. Mechanical strength decay evaluation of excavation unloaded rock mass under freeze-thaw conditions. *Appl. Sci.* **2022**, *12*, 12205. [CrossRef]
9. Chen, X.; Jiang, H.; Chen, L.; Du, W.; Gong, S. Experimental study on creep characteristics of unloaded rock masses for excavation of rock slopes in cold areas. *Appl. Sci.* **2023**, *13*, 3138. [CrossRef]
10. Zhu, Y.; Li, P.; Wang, P.; Mei, C.; Ren, H.; Wang, X. Mechanical characteristics of pre-peak unloading damage and mechanisms of reloading failure in red sandstone. *Appl. Sci.* **2022**, *12*, 13046. [CrossRef]
11. Martin, C.D.; Chandler, N.A. The progressive fracture of Lac du Bonnet granite. *Int. J. Rock Mech. Min. Sci. Geomech. Abstr.* **1994**, *31*, 643–659. [CrossRef]
12. Zong, Y.; Han, L.; Wei, J.; Wen, S. Mechanical and damage evolution properties of sandstone under triaxial compression. *Int. J. Min. Sci. Technol.* **2016**, *26*, 601–607. [CrossRef]
13. Li, J.; Duan, K.; Meng, H.; Wang, J.; Zhang, Q.; Wang, L. On the mechanical properties and failure mechanism of conglomerate specimens subjected to triaxial compression tests. *Rock Mech. Rock Eng.* **2022**, *56*, 973–995. [CrossRef]
14. Huang, R.Q.; Huang, D. Experimental research on affection laws of unloading rates on mechanical properties of Jinping marble under high geostress. *Chin. J. Rock Mech. Eng.* **2010**, *29*, 21–33.
15. Li, J.L.; Wang, R.H.; Jiang, Y.Z.; Liu, J.; Chen, X. Experimental study of sandstone mechanical properties by unloading triaxial tests. *Chin. J. Rock Mech. Eng.* **2010**, *29*, 2034–2041.
16. Qiu, S.L.; Feng, X.T.; Zhang, C.Q.; Yang, J.B. Experimental research on mechanical properties of deep marble under different initial damage levels and unloading paths. *Chin. J. Rock Mech. Eng.* **2012**, *31*, 1686–1697.
17. Deng, H.F.; Zhou, M.L.; Li, J.L.; Hu, Y.Y.; Xiao, Z.Y.; Wang, Y. Experimental research on unloading triaxial rheological mechanical properties of sandy mudstone. *Rock Soil Mech.* **2016**, *37*, 315–322. [CrossRef]
18. Wang, L.H.; Niu, C.Y.; Zhang, B.W.; Ma, Y.B.; Yin, S.J.; Xu, X.L. Experimental study on mechanical properties of deep-buried soft rock under different stress paths. *Chin. J. Rock Mech. Eng.* **2019**, *38*, 973–981.

19. Li, J.; Huang, T.; Zhang, H.; Deng, H. Research review and prospect in experimental studies for unloading rock mass mechanics. *J. Chin. Three Gorges Univ.* **2022**, *44*, 1–13.

20. Lin, H.; Liu, J.; Yang, J.; Ran, L.; Ding, G.; Wu, Z.; Lyu, C.; Bian, Y. Analysis of damage characteristics and energy evolution of salt rock under triaxial cyclic loading and unloading. *J. Energy Storage* **2022**, *56*, 106145. [CrossRef]

21. Eberhardt, E.; Stead, D.; Stimpson, B.; Read, R.S. Identifying crack initiation and propagation thresholds in brittle rock. *Can. Geotech. J.* **1998**, *35*, 222–233. [CrossRef]

22. Eberhardt, E.; Stead, D.; Stimpson, B. Quantifying progressive pre-peak brittle fracture damage in rock during uniaxial compression. *Int. J. Rock Mech. Min. Sci.* **1999**, *36*, 361–380. [CrossRef]

23. Liu, D.; Jiang, S.; Tang, Y. Mechanical properties of metasandstone under uniaxial graded cyclic loading and unloading. *Appl. Sci.* **2022**, *12*, 6310. [CrossRef]

24. Meng, Q.B.; Liu, J.F.; Ren, L.; Pu, H.; Chen, Y.L. Experimental study on rock strength and deformation characteristics under triaxial cyclic loading and unloading conditions. *Rock Mech. Rock Eng.* **2021**, *54*, 777–797. [CrossRef]

25. Xiao, F. Study on True-Triaxial Unloading Behaviors and Failure Mechanism of Damaged Sandstone. Doctoral Thesis, Chongqing University, Chongqing, China, 2021.

26. Meng, Q.B.; Qian, W.; Pu, H.; Huang, B.X.; Wang, C.K. Experimental mechanical properties of damaged and fractured rock samples. *Chin. J. Rock Mech. Eng.* **2020**, *39*, 1534–1546.

27. Wang, P.; Zhu, Y.; Feng, T. Test and analysis of sandstone damage-weakening underloading-unloading-loading. *J. Chin. Coal. Soc.* **2016**, *12*, 2960.

28. Ren, H.; Zhu, Y.; Wang, P.; Yu, W.; Huang, Z. Experimental analysis of mechanical properties of reloading after initial damage of white sandstone specimens. *Miner. Eng. Res.* **2019**, *34*, 23.

29. Zhu, Y.; Ren, H.; Wang, P. Mechanical properties and failure mechanism of damaged limestone under uniaxial reloading. *J. Harbin Inst. Technol.* **2021**, *53*, 119–126.

30. Niu, S.J.; Jing, H.W.; Yang, X.X.; Yang, S.Q. Experimental study of strength degradation law of surrounding rock in fractured zone of deep roadway. *Chin. J. Rock Mech. Eng.* **2012**, *31*, 1587–1596.

31. Okubo, S.; Fukui, K.; Sugita, T. Study on strength recovery of loosen zone. *Shigen-to-Sozai* **2001**, *117*, 631–638. [CrossRef]

32. Hashiba, K.; Okubo, S.; Fukui, K. Strength recovery of weak sedimentary rocks from complete failure. In Proceedings of the 38th Symposium on Rock Mechanics, Tokyo, Japan, 8–9 January 2009; Japan Society of Civil Engineers: Tokyo, Japan, 2009; pp. 161–166.

33. Lei, M.; Hashiba, K.; Fukui, K. Study on compaction characteristics and strength recovery of rock in the loosen zone. *Chin. J. Rock Mech. Eng.* **2011**, *30*, 2710–2719.

34. Martin, C.D. Seventeenth Canadian Geotechnical Colloquium: The effect of cohesion loss and stress path on brittle rock strength. *Can. Geotech. J.* **1997**, *34*, 698–725. [CrossRef]

35. Wang, Y.; Li, X.; Wu, Y.F.; Pen, Y.X.; Li, D.D. Research on relationship between crack initiation stress leve.and brittleness indices for brittle rocks. *Chin. J. Rock Mech. Eng.* **2014**, *33*, 264–275. [CrossRef]

36. Ni, J.C.; Chen, Y.T.; Chen, X.X. Seismic moment tensor and its inversion. *Seismol. Geomagn. Obs. Res.* **1991**, *5*, 1–17.